




# Anharmonic phonon renormalization and thermal transport in the type-I $\text{Ba}_8\text{Ga}_{16}\text{Sn}_{30}$ clathrate from first principles

Masato Ohnishi <sup>1,\*</sup>, Terumasa Tadano <sup>2,3</sup>, Shinji Tsuneyuki<sup>4,5</sup> and Junichiro Shiomi <sup>1,6,†</sup>

<sup>1</sup>*Department of Mechanical Engineering, The University of Tokyo, 7-3-1 Hongo, Bunkyo-ku, Tokyo 113-8656, Japan*

<sup>2</sup>*Research Center for Magnetic and Spintronic Materials, National Institute for Materials Science (NIMS), 1-2-1 Sengen, Tsukuba, Ibaraki 305-0047, Japan*

<sup>3</sup>*Elements Strategy Initiative Center for Magnetic Materials, National Institute for Materials Science (NIMS), 1-2-1 Sengen, Tsukuba, Ibaraki 305-0047, Japan*

<sup>4</sup>*Department of Physics, The University of Tokyo, 7-3-1 Hongo, Bunkyo-ku, Tokyo 113-0033, Japan*

<sup>5</sup>*Institute for Solid State Physics, The University of Tokyo, 5-1-5 Kashiwanoha, Kashiwa, Chiba 277-8581, Japan*

<sup>6</sup>*Institute of Engineering Innovation, The University of Tokyo, 2-11 Yayoi, Bunkyo-ku, Tokyo 113-0032, Japan*



(Received 27 February 2021; revised 23 April 2022; accepted 17 June 2022; published 8 July 2022)

Effects of strong phonon anharmonicity of a type-I clathrate  $\text{Ba}_8\text{Ga}_{16}\text{Sn}_{30}$  induced by the quadruple-well potential of guest atoms were investigated. Phonon transport including a coherent interbranch component was analyzed using a first-principles-based self-consistent phonon (SCP) theory that gives temperature-dependent harmonic interatomic force constants and by solving off-diagonal components of group velocity operator. Experimentally observed thermal conductivities have been reasonably reproduced by considering both lattice and electron contributions. Through the analysis with the SCP theory, we found that hardening of guest modes leads to an increase in lattice thermal conductivity at frequencies below those of framework-dominant flat modes ( $<40\text{ cm}^{-1}$ ), which finally results in the slow decay of the total lattice thermal conductivity with increasing temperature. Detailed analyses revealed that the increase in lattice thermal conductivity at low frequency is attributed to (a) the increase in both group velocities and lifetimes of phonon modes located at frequencies below that of the flat guest modes and (b) abnormal increase in lifetimes of phonon modes located between frequencies of the flat guest and framework modes with increasing temperature.

DOI: [10.1103/PhysRevB.106.024303](https://doi.org/10.1103/PhysRevB.106.024303)

## I. INTRODUCTION

Phonon-glass electron-crystal [1] is a concept of ideal thermoelectric properties of crystal materials. Materials such as skutterudite [2], perovskite [3,4], and clathrate compounds [5,6] composed of cages and guest atoms are expected to realize this concept. In these materials, it is expected that phonons are significantly scattered by guest atoms while electrons can transport in the framework without significant scattering. Because a large free space of guest atoms is preferred to enhance phonon scattering by guest atoms [7,8], type-I clathrates [9] composed of Weaire-Phelan structures [10], which divide space into cage structures with a large volume, may be the most promising materials. Indeed, they exhibit various intriguing phonon properties such as a glasslike plateau of temperature-dependent thermal conductivity  $\kappa(T)$  at low temperatures [7,11,12], significant hardening of guest modes with temperature [13–15], and weak temperature dependence of  $\kappa(T)$  at high temperatures [7,12,16].

Recent theoretical works on clathrates have revealed the basic effects of the guest atoms on phonon properties. The weak interaction between guest atoms and the framework results in flat bands, and the flat guest bands affect phonon

properties in different manners. The main impact of the flat guest bands on phonon properties is to suppress phonon relaxation times in a wide range of frequencies [17–19]. It may be straightforward to understand that the flattening of bands increases the scattering phase space (SPS) of phonons and decreases their relaxation time. In addition to SPS, the three-phonon coupling matrix represented by eigenvalues, polarization vectors, and atomic masses (described in the Methodology section in detail) among scattered phonons also has a vital role in decreasing the relaxation time according to detailed analyses on type-I  $\text{Ba}_8\text{Ga}_{16}\text{Ge}_{30}$  (BGGe) [19]. As for phonon group velocity, while hybridization of the guest and framework modes decreases group velocities, theoretical works [18,19] have shown that the effect on group velocities is secondary. It has also been found that the glasslike plateau of temperature-dependent thermal conductivity at low temperature can be attributed to thermal excitation of phonons with higher frequencies than those of flat bands [20]. It may be interesting to note that the glasslike plateau is not a direct consequence of phonon anharmonicity because the effect of thermal excitation is relatively enhanced by the flat guest bands that suppress the contribution of low-frequency phonons to heat transport. Therefore, an in-depth understanding of the phenomena observed at high temperatures, e.g., the weak temperature dependence of thermal conductivity, should give us more knowledge on phonon anharmonicity.

\*ohnishi@photon.t.u-tokyo.ac.jp

†shiomi@photon.t.u-tokyo.ac.jp

In this paper, we investigate the effects of strong phonon anharmonicity at high temperatures from first-principles calculations. Type-I clathrate  $\text{Ba}_8\text{Ga}_{16}\text{Sn}_{30}$  (BGSn), which has a remarkably strong anharmonicity [21] compared with other off-center clathrates such as Sr- and Eu-filled Ge clathrates  $[(\text{Sr}/\text{Eu})_8\text{Ga}_{16}\text{Ge}_{30}]$  [22], is mainly analyzed. Furthermore, type-I  $\text{Ba}_8\text{Ga}_{16}\text{Si}_{30}$  (BGSi), which has much weaker anharmonicity than BGSn, is analyzed to highlight the effect of strong anharmonicity in BGSn. Quartic phonon anharmonicity is incorporated to obtain temperature-dependent effective second-order interatomic force constants (IFCs) using a self-consistent phonon (SCP) theory [23,24]. In addition to the phonon transport considered by the Peierls-Boltzmann transport equation (BTE), the coherent interbranch component is also considered by employing the so-called unified theory formulated by Simoncelli *et al.* [25]. These analyses reveal that lattice thermal conductivity can be increased by hardening of flat-band guest modes, and the coherent thermal transport is not negligible above a few hundred degrees kelvin. Because the hardening of guest modes significantly increases thermal conductivity at low frequencies, it leads to intriguing phenomena such as stronger suppression of thermal conductivity due to nanostructuring at higher temperatures.

## II. METHODOLOGY

### A. Interatomic force constants

Type-I clathrate BGSn with a highly symmetric structure ( $Pm\bar{3}n$  space group) was analyzed in this paper. For the sake of comparison, type-I BGSi, which has much weaker anharmonicity than type-I BGSn, was also analyzed. In both structures, all  $16i$  sites are occupied by gallium atoms, and  $6c$  and  $24k$  sites are occupied by tin or silicon atoms. IFCs were obtained with first-principles calculations using the Vienna *ab initio* Simulation Package (VASP) [26]. The Perdew-Burke-Ernzerhof exchange-correlation functional [27] with the projector augmented wave potential [28,29] was employed in all calculations. The cutoff energies were set at 330 and 340 eV for BGSi and BGSn, respectively. The lattice constants of the clathrates were optimized using a  $4 \times 4 \times 4$  Monkhorst-Pack  $\mathbf{k}$ -mesh, where  $\mathbf{k}$  is the wavevector. The optimized lattice constants were 10.60 Å for BGSi and 11.90 Å for BGSn. While the former value is in excellent agreement with an experimental value (10.59 Å [30]), the latter is slightly larger than an experimental value (11.69 Å [31]). While the lattice thermal conductivity may depend on the value of the lattice constant [20], the values obtained through calculations of this paper are used herein.

To obtain anharmonic IFCs of BGSn, many structures in which atoms were randomly displaced were prepared, while harmonic IFCs were obtained through a finite displacement approach [32] with a displacement of 0.01 Å. Here,  $2 \times 2 \times 2$  supercells, containing 432 atoms, were used for BGSn to calculate IFCs, while primitive cells were used for BGSi to reduce the computational cost. First, first-principles molecular dynamics (MD) simulations with a primitive cell were performed at a temperature of 500 K with a time step of 1.0 fs and a  $2 \times 2 \times 2$  Monkhorst-Pack  $\mathbf{k}$ -mesh. The temperature was controlled using a velocity-scaling algorithm during the

first few hundred femtoseconds of the simulation and then via the Nosé-Hoover algorithm [33]. After confirming that atomic vibrations had stabilized, the structures were extracted every 50 fs, and every atom was displaced along a random direction with a maximum magnitude of 0.1 Å to ensure that no two structures were correlated. More than 120 structures were prepared from the trajectory of the MD simulation. Using the set of atomic displacements and forces, anharmonic IFCs were calculated up to the sixth order using the least absolute shrinkage and selection operator solved using the coordinate descent method [34], while the harmonic IFCs were fixed with those obtained by the finite displacement method. The cutoffs of IFCs were set to be 20.6 and 5.29 Å for harmonic and other orders, respectively, and interactions of atoms were considered up to three, two, and two body for fourth-, fifth-, and sixth-order IFCs, respectively. In the case of BGSn, after the calculation of IFCs with the primitive cell, IFCs were calculated with a  $2 \times 2 \times 2$  supercell in a similar manner, while IFCs obtained with the primitive cell were used to perform a MD simulation for the supercell. More than 180 randomly displaced structures were prepared to calculate forces on atoms, and a  $2 \times 2 \times 2$  Monkhorst-Pack  $\mathbf{k}$ -mesh was employed for first-principles calculations. Temperature-dependent harmonic IFCs were obtained by using the SCP theory [20,23] which modifies harmonic IFCs with the effect of quartic anharmonicity. The SCP calculations were performed at the  $\Gamma$  point ( $\mathbf{q} = 0$ ), and eigenvalues and eigenvectors at arbitrary  $\mathbf{q}$  points were obtained via Fourier interpolation. Because only short-range interactions contribute to anharmonic terms, the  $\Gamma$  point calculation should be sufficient for this calculation. For all simulations based on the SCP theory, off-diagonal components of self-energy and, thus, polarization mixing were considered in this paper. Also, while it is, in principle, possible to update the atomic positions at each temperature within a SCP formulation [35], we do not consider this effect in this paper due to computational limitations and assume that the atomic positions do not change from their equilibrium positions at 0 K. Notwithstanding, the present SCP method should be useful for understanding anharmonic lattice dynamics and thermal transport of BGSn at relatively high temperatures above  $\sim 100$  K, where the kinetic energy surpasses the depth of the multiple-well potential inside the host cage and thereby makes the effect of off-centering motion less significant.

### B. Lattice thermal conductivity

Using the obtained harmonic and cubic IFCs, lattice thermal conductivity  $\kappa_L$  without including the coherent part  $\kappa_p$  was calculated by solving the Peierls-BTE, which is associated with diagonal terms of the group velocity operator [36]. Considering the second-order perturbation within the single-mode relaxation approximation, the linewidth due to the three-phonon scattering for phonon mode  $q$  is derived as

$$\Gamma_q = \frac{\pi}{16N} \sum_{q_1, q_2} |V_3(-q, q_1, q_2)|^2 [(n_1 + n_2 + 1) \times \delta(\omega_q - \omega_1 - \omega_2) - 2(n_1 - n_2)\delta(\omega_q - \omega_1 + \omega_2)], \quad (1)$$

where the subscripts ( $i = 1, 2$ ) denote phonon modes contributing to the scattering of the target mode  $q$ ,  $n_i$  is the Bose-Einstein distribution function,  $\omega_i$  is the phonon frequency,  $N$  is the number of  $\mathbf{q}$  points, and  $\pm q = (\pm \mathbf{q}, s)$  with  $\mathbf{q}$  and  $s$  being the wavevector and branch index, respectively. The three-phonon coupling matrix element  $V_3$  is given by

$$V_3(q, q_1, q_2) = \left( \frac{\hbar}{\omega \omega_1 \omega_2} \right)^{1/2} \sum_{\mathbf{R}_i, l_i, p_i} \psi_{0l_0, \mathbf{R}_i l_i, \mathbf{R}_2 l_2}^{p_0 p_1 p_2} \times \frac{\mathbf{e}_{l_0}^{p_0}(\mathbf{q}) \mathbf{e}_{l_1}^{p_1}(\mathbf{q}_1) \mathbf{e}_{l_2}^{p_2}(\mathbf{q}_2)}{\sqrt{M_{l_0} M_{l_1} M_{l_2}}} \times \exp[i(\mathbf{q} \cdot \mathbf{R}_0 + \mathbf{q}_1 \cdot \mathbf{R}_1 + \mathbf{q}_2 \cdot \mathbf{R}_2)], \quad (2)$$

where  $\hbar$  is the reduced Planck constant,  $\mathbf{R}_i$  is the position of the primitive cell,  $l_i$  is the atom index,  $p_i$  is the direction of the displacement of atom  $l_i$ ,  $M$  is the atomic mass,  $\Psi$  is the cubic IFCs, and  $\mathbf{e}(q)$  is the eigenvector of the mode  $q$ . The phonon lifetime due to three-phonon scattering  $\tau_{pp}$  is given by  $\tau_{pp}(q) = 1/(2\Gamma_q)$ . The total phonon lifetime of mode  $q$  is obtained with Matthiessen's rule:  $\tau_q^{-1} = \tau_{q, pp}^{-1} + \tau_{q, iso}^{-1} + \tau_{q, b}^{-1}$ , where  $\tau_{q, iso}^{-1}$  is the scattering rate due to isotopes [37], and  $\tau_{q, b}^{-1} = 2|\mathbf{v}_q|/L_g$  due to boundary of grains with an effective diameter  $L_g$ , respectively. Finally, the Peierls term is calculated as  $\kappa_p^{\alpha\beta, scp}(T) = (NV)^{-1} \sum_q c_q(T) v_q^\alpha(T) v_q^\beta(T) \tau_q(T)$  using IFCs modified with the SCP theory. Here,  $V$  is the volume of the primitive unit cell,  $c$  is the mode specific heat,  $v$  is the group velocity, and  $\alpha$  and  $\beta$  are the Cartesian directions. In this analysis, the result for  $\alpha = \beta$  was taken because the type-I clathrates used were isotropic.

Because linewidths of phonons may be larger than interbranch spacings in some branches of BGSn, the contribution of interbranch coherent tunneling to heat transport may not be negligible. Therefore, the coherent component, corresponding to the nondiagonal terms of the heat flux operator, was calculated by the unified theory [25,36]. Its contribution can be obtained as

$$\kappa_c^{\alpha\beta} = \frac{\hbar^2}{k_B T^2 V N} \sum_{\mathbf{q}} \sum_{s_1 \neq s_2} \frac{\omega_1 + \omega_2}{4} V_{12}^\alpha(\mathbf{q}) V_{21}^\beta(\mathbf{q}) \times \frac{\omega_1 n_1 (n_1 + 1) + \omega_2 n_2 (n_2 + 1)}{(\omega_1 - \omega_2)^2 + (\Gamma_1 + \Gamma_2)^2} (\Gamma_1 + \Gamma_2), \quad (3)$$

where  $k_B$  is the Boltzmann constant. The subscripts (1 and 2) denote the phonon modes ( $\mathbf{q}, s_1$ ) and ( $\mathbf{q}, s_2$ ), respectively. The generalized group velocity operator  $V(q)$  is given as

$$V_{12}(\mathbf{q}) = \frac{1}{\omega_1 + \omega_2} \left\langle \mathbf{e}(\mathbf{q}, s_1) \left| \frac{\partial D(\mathbf{q})}{\partial \mathbf{q}} \right| \mathbf{e}(\mathbf{q}, s_2) \right\rangle, \quad (4)$$

where  $D(\mathbf{q})$  is the dynamical matrix, which includes the anharmonic renormalization from the SCP theory.

Both for the Peierls and coherent contribution  $\kappa_L$  were calculated with  $N_q \times N_q \times N_q$   $\mathbf{q}$ -meshes, where  $N_q$  was varied from 11 to 19, and final values were obtained by a linear extrapolation with respect to  $N_q^{-1}$ . The tetrahedron method [38] was used for the integration over the Brillouin zone. For the above simulations to obtain IFCs and  $\kappa_L$  ( $= \kappa_p^{scp} + \kappa_{off}$ ), the ALAMODE package [3,39] was employed.

### C. Electron thermal conductivity

Because electron contribution to thermal transport may not be negligible in BGSn above room temperature [40], electron thermal conductivity  $\kappa_{el}$  was also calculated within the constant relaxation time approximation employing BOLTZTRAP2 [41]. Details are also documented in Sec. I in the Supplemental Material (SM) [42]. Electron band structures were calculated using VASP in basically the same manner as that for the phonon analysis. The  $\mathbf{k}$ -mesh density was set to  $20 \times 20 \times 20$  for electron analysis, with which the convergence of electron properties such as electrical conductivity was confirmed. The carrier concentration is set to be an experimentally observed value  $3.2 \times 10^{18} \text{ cm}^{-3}$  [31], and the electron relaxation time was determined as 1.26 fs to reproduce the electrical conductivity at room temperature [31].

The principal reason to consider electron contribution is to reproduce an increase in thermal conductivity above room temperature due to the bipolar effect [40]. Although the temperature at which the bipolar effect becomes distinct strongly depends on the magnitude of the bandgap, the accurate investigation of the bandgap of clathrates is challenging. This difficulty comes from a unique feature of clathrates as well as a general problem of semilocal density functionals for exchange and correlation [43]. In the framework of clathrate compounds, atoms can be placed with different combinations of sites and elements, namely, site occupancy factors, even with the same composition of elements, and their electronic states depend on the placement of atoms [44,45]. While it may be possible to estimate a plausible bandgap by considering the effect of temperature and taking an ensemble average for possible structures [46–48] and carefully selecting an exchange-correlation functional, we simply modified the magnitude of the bandgap by manually adjusting the energy of the conduction bands in this analysis. This adjustment of the bandgap modifies only the threshold temperature of bipolar effect but not the increasing rate of electron thermal conductivity with temperature, as shown in Fig. S1 in the SM [42].

## III. RESULTS AND DISCUSSIONS

### A. Temperature-dependent harmonic properties

Because type-I BGSn has a quadruple-well potential on the Ba guest atom at the  $6d$  site, the quartic lattice anharmonicity and the associated temperature renormalization of phonon frequency are significant. Figure 1(a) shows a potential energy surface (PES) of the lowest optical mode at the  $\Gamma$  point ( $T_{2g}$  mode), which is dominated by the guest atom. The deviation of the stable positions of the guest atom from the cage center was 0.84 Å which exceeded an experimental value of 0.43 Å [31]. This overestimation should be because of the larger lattice constant as mentioned in Sec. II A. The depth of the quadruple-well potential was 5.6 meV/atom (0.31 eV/unit cell), which corresponds to 66 K. Decomposed anharmonic contributions up to the sixth order show that even-order potentials dominate the potential on the guest atom at the  $6d$  site, while the odd-order potentials become zero because of the symmetry. By employing the SCP theory, harmonic IFCs [blue dotted lines in Fig. 1(a)] were gradually renormalized

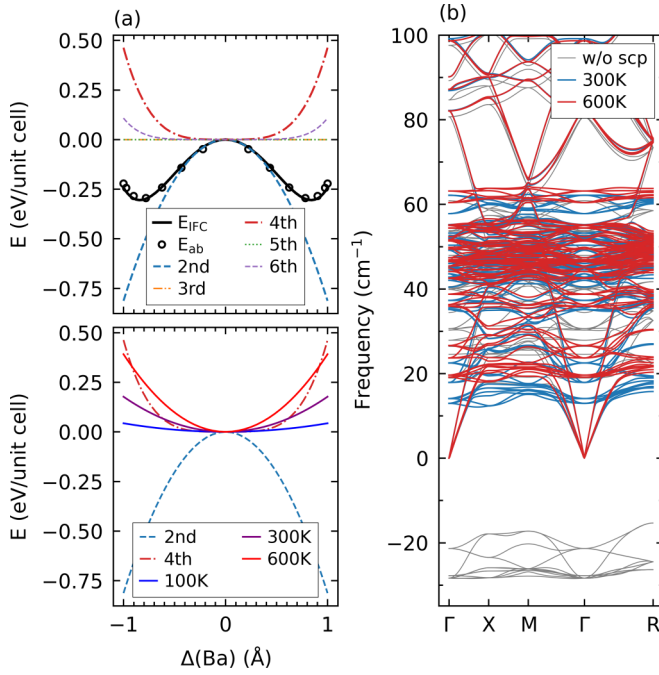


FIG. 1. Temperature-dependent harmonic phonon properties of type-I BGSn. (a) Potential energy surface (PES) of the lowest guest mode at the  $\Gamma$  point ( $T_{2g}$  mode). In the top panel, black circles show values obtained directly from first-principles calculations, and the black line shows data obtained through the interatomic force constants. Colored lines show PESs decomposed up to sixth order. In the bottom panel, solid lines show temperature-dependent harmonic potentials. (b) Phonon dispersions obtained without (gray) and with (blue and red) considering the quartic anharmonicity. The latter is shown for 300 and 600 K.

by the quartic potential (red dash-dotted line) with increasing the temperature. Under the assumption used in this analysis, if guest atoms vibrate on the cage center in a positive harmonic potential, the SCP calculation is converged only above a certain temperature at which the effective harmonic potential including the effect of the quartic potential becomes positive. In this paper, the SCP calculation is converged at 100 K or above for the type-I BGSn. While eigenvalues have imaginary values without considering the effect of quartic anharmonicity, an inclusion of quartic anharmonicity lifts imaginary frequencies to positive values, as shown in Fig. 1(b). Following the hardening of phonon modes, the frequency of the  $T_{2g}$  mode (the lowest optical mode) is varied from  $6.2 \text{ cm}^{-1}$  at 100 K to  $13 \text{ cm}^{-1}$  at 300 K, as shown in Fig. S2(a) in the SM [42]. The experimentally measured frequencies of the  $T_{2g}$  mode are  $16 \text{ cm}^{-1}$  at 100 K and  $19 \text{ cm}^{-1}$  at 300 K [15,49]. This comparison shows that, while the discrepancy between the experimental and theoretical values is distinct at low temperatures, it becomes smaller with increasing temperature. The underestimation of the frequencies of the rattling modes may be attributed to the overestimation of the lattice constant. Another possibility is that the instability of the highly symmetric structure used in this paper [44] may soften some phonon modes including the guest modes. Indeed, our simulation with a lower symmetric but more stable structure shows higher frequencies of the guest modes and a larger

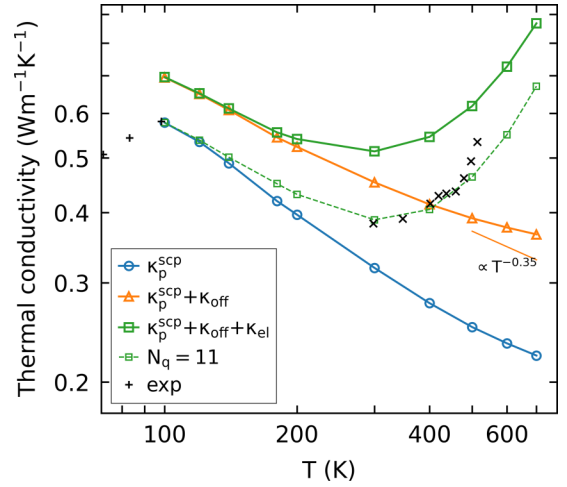


FIG. 2. Temperature-dependent thermal conductivity of type-I BGSn. Blue, orange, and green lines denote data including the nondiagonal Peierls contribution ( $\kappa_p^{\text{SCP}}$ ), interbranch coherent contribution ( $\kappa_c$ ), and electron contribution ( $\kappa_{\text{el}}$ ), respectively. Data on the dotted line were obtained with  $11 \times 11 \times 11$   $\mathbf{q}$ -mesh, while other data were with the linear extrapolation with respect to  $N_q^{-1}$ . Black markers show experimental data of single crystals obtained from Ref. [31] for temperatures  $< 100$  K and Ref. [40]  $> 300$  K. Note that the experiments were measured by different methods: a steady-state method  $< 100$  K and laser flash  $> 300$  K.

split of their frequencies, which agree with the experimental data, while we employed the symmetric structure for the simplicity in this paper. Calculation of partial density of states (DOS) shows that flat modes lying at low frequency can be divided into two groups, as shown in Figs. S2(b) and S2(c) in the SM [42], which show clearer phonon dispersion and DOS. The flat bands  $\sim 20 \text{ cm}^{-1}$  are dominated by Ba guest atoms, while flat bands  $\sim 40\text{--}60 \text{ cm}^{-1}$  are dominated by the framework. We will show that phonon modes located at a frequency below the flat guest bands and phonon modes located between the flat guest and framework modes play an important role in realizing intriguing phonon properties of type-I BGSn.

## B. Temperature-dependent thermal conductivity

Using the temperature-dependent effective harmonic IFCs and (bare) cubic IFCs, thermal conductivities of type-I BGSn were calculated. Because  $\kappa_L$  linearly increased with decreasing  $N_q^{-1}$  both for Peierls and coherent contributions [50], as shown in Fig. S3 in the SM [42], final values were obtained by a linear extrapolation with respect to  $N_q^{-1}$ . While SCP calculations were not converged when the temperature is below 100 K available data are shown in Fig. 2. Data on solid lines were obtained by the extrapolation, while those of the dotted line were for  $N_q = 11$ . To reproduce the increase of thermal conductivity above 300 K observed in the experiment [40], the electronic bandgap was modified from 0.045 to 0.06 eV for the extrapolated data and to 0.15 eV for data of  $N_q = 11$ . The result shows that total thermal conductivities including Peierls, coherent, and electron contributions (squares with solid line) overestimate experimental data in the overall temperature, while data obtained with  $N_q = 11$

can reproduce them. Possible missing factors in this analysis which reduce thermal conductivity may be dynamical disorder of guest atoms [16,51], four-phonon scattering [52,53], or thermal expansion [20,48]. While the dynamical disorder mainly affects thermal conductivity at low temperatures, the other two factors should decrease thermal conductivities in the overall temperature. We would like to note that  $N_q = 11$  is not a small size of  $\mathbf{q}$ -mesh compared with previous calculations [20,48]. This indicates that it is still challenging to reveal all the physics behind the small thermal conductivity of clathrate compounds. As for the Coulomb interaction among guest ions, we did not consider the dipole-dipole interaction beyond the  $2 \times 2 \times 2$  supercell in this paper, while it may affect thermal conductivity at low temperatures [54,55].

We would like to also comment on the difference between the temperature dependences of thermal conductivity of amorphous structures and off-center type-I clathrates, that is, that of glasses and the glasslike dependence. Here,  $\kappa_L$  of glasses keeps increasing in all temperature regions except for at low temperatures (typically  $\sim 10$  K), at which its temperature dependence is absent, and at temperatures above the high temperature limit (typically  $\sim 100$  K), at which it saturates a certain value [56]. The same temperature dependence has been observed in type-I clathrate compounds with large off-center distances such as  $\text{Sr}_8\text{Ga}_{16}\text{Ge}_{30}$  [16] and  $\text{Eu}_8\text{Ga}_{16}\text{Ge}_{30}$  [57] as well as BGSn [31]. While we targeted temperatures  $> 100$  K, at which equilibrium positions of guest atoms should be considered as the center of the cage structure, our results in Fig. 2 and experimental data of type-I BGSn [31,40] show that  $\kappa_L$  of off-center type-I clathrates can decrease after taking the maximum value at  $\sim 100$  K. Our simulations reveal the difference of the physics on heat transport at high temperatures between amorphous and off-center type-I clathrates. While heat transport is dominated by diffusons and locons in amorphous systems, it is still dominated by propagons ( $\kappa_p^{\text{scp}}$  in this paper) at high temperatures ( $> 100$  K) in off-center type-I clathrates. Because the temperature dependence of the total  $\kappa_L$  is dominated by competing temperature dependences of propagons and other contributions, diffusons and locons (dominant factors of  $\kappa_{\text{off}}$  in this paper), when propagons mainly contribute to  $\kappa_L$ , the total  $\kappa_L$  decreases due to increase in phonon-phonon scattering with increasing temperature. It may be interesting to think that, while thermal properties of off-center clathrates are glasslike at low temperatures, they turn back to crystal at high temperatures because of their high-order anharmonicity.

While the physics may still be unveiled, our calculations show intriguing thermal properties of clathrate compounds: (a) slow reduction of lattice thermal conductivity with temperature ( $\propto T^{-0.35}$ ), (b) significant contribution of coherent component, and (c) sharp increase in thermal conductivity because of electronic contribution. While the increase of  $\kappa_{\text{el}}$  might be noticeable, its effect simply can be attributed to the bipolar effect (see Fig. S1 in the SM [42]). We will, therefore, focus on more intriguing phenomena of phonon transport below.

### C. Modal thermal conductivity

To gain insight into the slow decay of  $\kappa(T)$  with temperature, spectral and cumulative  $\kappa_p^{\text{scp}}(T)$  of type-I BGSi

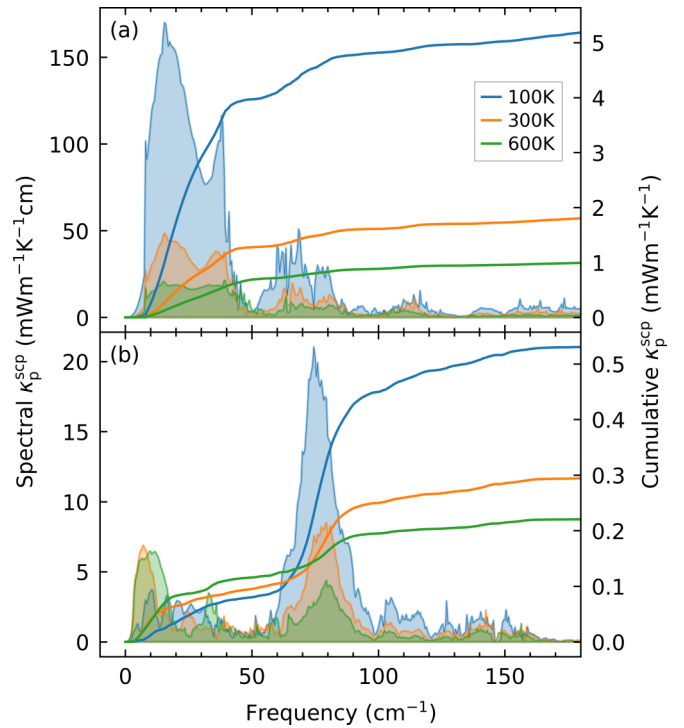


FIG. 3. Spectral and cumulative lattice thermal conductivities of (a) BGSi and (b) BGSn at different temperatures. The contribution of interbranch coherent component is not considered.

and BGSn are compared in Fig. 3. In usual single-crystal materials, including type-I BGSi, which do not have strong phonon anharmonicity, modal thermal conductivity decreases with increasing temperature at most frequencies because of the enhancement of phonon-phonon scattering, as shown in Fig. 3(a). In type-I BGSn, interestingly, thermal conductivities at low frequency ( $< 50 \text{ cm}^{-1}$ ) increase with the temperature, as shown in Fig. 3(b). This increase of thermal conductivity of low-frequency phonons partially compensates the decrease of heat transport of higher-frequency phonons ( $> 50 \text{ cm}^{-1}$ ), leading to the weak temperature dependence. Thermal conductivity divided into different frequency ranges show distinctly different features in BGSi and BGSn, as shown in Fig. S4 in the SM [42]. In BGSi, lower-frequency phonons ( $< 50 \text{ cm}^{-1}$ ) dominate the total heat transport at low temperatures, while contributions of higher-frequency phonons ( $> 50 \text{ cm}^{-1}$ ) do not change significantly with temperature because of their small contribution. In BGSn, however, while middle-frequency ( $50\text{--}100 \text{ cm}^{-1}$ ) phonons dominate the total heat transport at low temperatures, the contribution of low-frequency phonons ( $< 20 \text{ cm}^{-1}$ ) increases with increasing temperature. For example, the contribution of phonons  $< 50 \text{ cm}^{-1}$  to the total  $\kappa_p^{\text{scp}}$  decreases from 74% at 100 K to 64% at 300 K for BGSi, while it increases from 15% at 100 K to 53% at 600 K for BGSn.

The increase in the contribution of low-frequency phonons with temperature may lead to an intriguing phenomenon. Nanostructuring is a technique to reduce phonon mean free path (MFP) and, thus, thermal conductivity for thermoelectric materials [58–60]. In materials with weak anharmonicity, nanostructuring decreases thermal conductivity more at

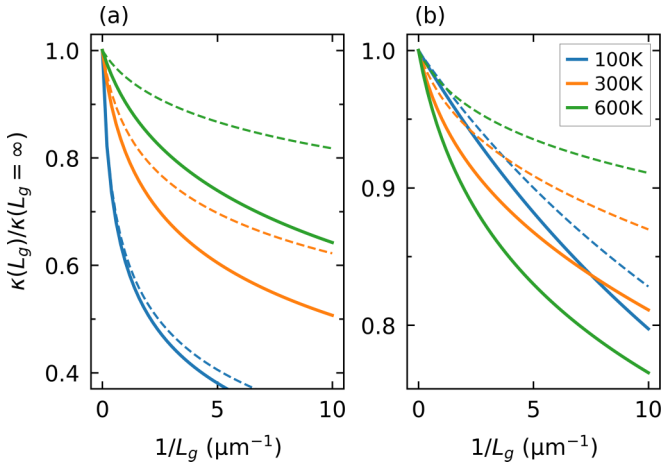


FIG. 4. Decrease in thermal conductivity due to nanostructuring for type-I (a) BGSi and (b) BGSn. Solid and dotted lines show data for  $\kappa = \kappa_p^{\text{scf}}(L_g)$  and  $\kappa = \kappa_p^{\text{scf}}(L_g) + \kappa_c + \kappa_{\text{el}}$ , respectively. It is assumed that  $\kappa_c$  and  $\kappa_{\text{el}}$  do not depend on the grain size  $L_g$ .

lower temperatures because of longer MFPs. Indeed,  $\kappa_p^{\text{scf}}$  of nanostructured BGSi decreases more with decreasing the grain size at lower temperatures, as shown by solid lines in Fig. 4(a). On the other hand, for BGSn, the reduction of  $\kappa_p^{\text{scf}}$  is weaker at lower temperatures in most cases because of the large contribution of high-frequency phonons, as shown in Fig. 4(b). This nontrivial trend qualitatively disappears in the total  $\kappa$  being outweighed by contribution from  $\kappa_c$  and  $\kappa_{\text{el}}$  when assuming them to be independent of  $L_g$ ; however, quantitatively, the deterioration of the nanostructuring effect with increasing temperature is significantly weakened in BGSn due to the strong anharmonicity.

#### D. Detailed analysis

To gain a deeper insight into the increase in thermal conductivity at low frequency with temperature, phonon properties were analyzed in more detail. While we call phonons at 0–50  $\text{cm}^{-1}$  the low-frequency phonons in the above discussion, Fig. S2(c) in the SM [42] [or Fig. 1(b)] shows that the frequency range of 0–50  $\text{cm}^{-1}$  is divided by the flat guest modes  $\sim 20 \text{ cm}^{-1}$ . Moreover, Fig. 3(b) shows that modal thermal conductivities increase continuously below 20  $\text{cm}^{-1}$  when the temperature is higher than 100 K, while those at 30–40  $\text{cm}^{-1}$  suddenly increase at  $>300 \text{ K}$ . The dip frequency of the spectral  $\kappa_p^{\text{scf}}(T)$  at 300 and 600 K of type-I BGSn  $\sim 20 \text{ cm}^{-1}$  clearly corresponds to the frequency range of flat guest modes, which is highlighted in Fig. S5 in the SM [42]. Figures 5(a) and 5(b) show that the flat guest modes, which are explicitly at 6–19  $\text{cm}^{-1}$  at 100 K, 12–22  $\text{cm}^{-1}$  at 300 K, and 19–27  $\text{cm}^{-1}$  at 600 K (see Fig. S5 in the SM [42]), have small lifetimes and group velocities, while phonons with smaller frequencies than those of the flat guest modes have much larger lifetimes and group velocities. (One can see an aggregation of data shifting to a higher frequency at the corresponding frequencies with increasing temperature.) Figure 5(a) also shows that phonon lifetimes at 30–40  $\text{cm}^{-1}$  increase from 300 to 600 K.

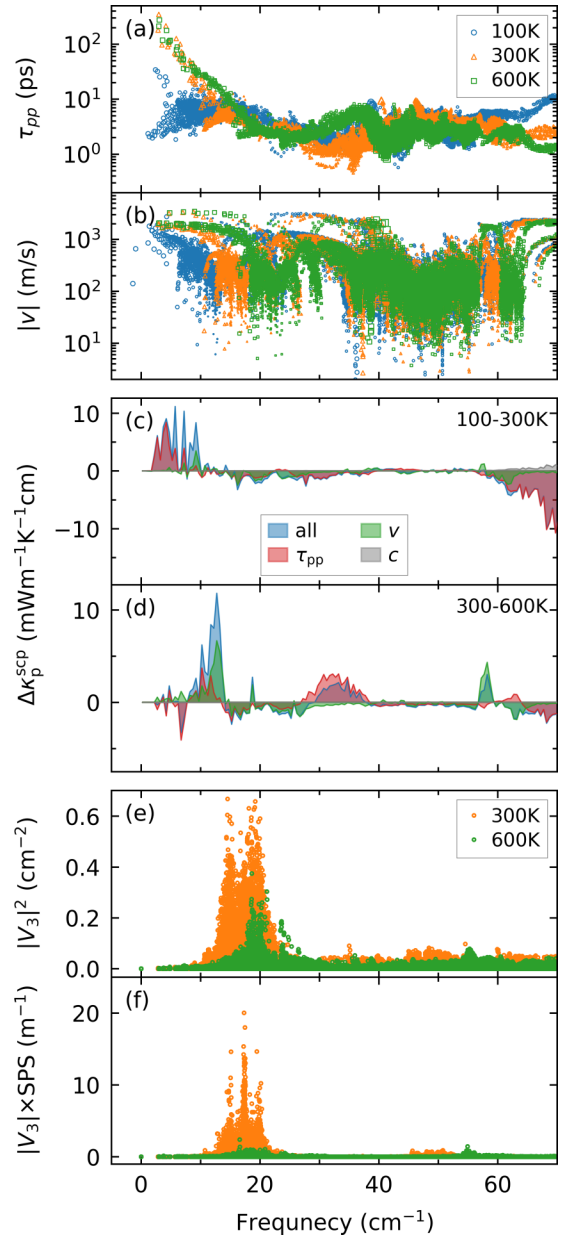


FIG. 5. Effect of hardening of flat guest bands in type-I BGSn. (a) Lifetime due to phonon-phonon scattering and (b) group velocity at different temperatures. (c) and (d) Change in modal thermal conductivities due to different phonon properties (group velocity, lifetime, and other factors) from (c) 100 to 300 K and (d) 300 to 600 K. Note that phonon frequencies depend on temperature in the analysis with the self-consistent phonon (SCP) theory. In (c) and (d), phonon frequencies at 100 and 300 K are taken, respectively. The magnitude of (e) the three-phonon coupling matrix element  $|V_3|^2$  and (f)  $|V_3|^2$  multiplied by the scattering phase space (SPS) term of the mode whose lifetime increases the most between 300 and 600 K (from 1.1 to 7.1 ps) that locates at 35  $\text{cm}^{-1}$  and  $\mathbf{q} = (0.0, 0.053, 0.37)$  at 300 K (see Fig. S5 in the SM [42]).

To investigate effects of the change in lifetimes and group velocities due to the hardening of guest modes, their effects were analyzed by calculating a virtual thermal conductivity:  $\kappa_{p,q}^{\text{scf}}(T_c, T_v, T_r) = c_q(T_c)v_q^2(T_v)\tau_q(T_r)$ . Each property, namely,

$c_q$ ,  $\mathbf{v}_q^2$ , and  $\tau_q$ , was calculated with the renormalized phonon dispersion, including the polarization vector and frequency, by the SCP theory and the Bose-Einstein distribution at a given temperature. The effect of a specific phonon property can be analyzed by changing the corresponding temperature in  $\kappa_{p,q}^{\text{SCP}}(T_c, T_v, T_\tau)$ . The corresponding phonon modes at different temperatures were identified to minimize the sum of inner products of all the corresponding eigenvectors at each  $\mathbf{q}$ -point. Figures 5(c) and 5(d) show changes in the modal thermal conductivity  $\kappa_{p,q}^{\text{SCP}}(T_c, T_v, T_\tau)$  due to each phonon property at lower temperatures (from 100 to 300 K) and higher temperatures (from 300 to 600 K), respectively. As shown in Fig. 5(c), the increase in thermal conductivity at 0–10  $\text{cm}^{-1}$  at the lower temperature range can be attributed mainly to increase in lifetime and partially to that in group velocity. From 100 to 300 K, the virtual  $\kappa_p^{\text{SCP}}$  at 0–10  $\text{cm}^{-1}$  increases by 2.6 times and by 24% because of the increase in lifetime and group velocity, respectively. While the total  $\kappa_p^{\text{SCP}}$  decreases because of the decrease in lifetimes at high frequency ( $>60 \text{ cm}^{-1}$ ), the increase in group velocities and lifetimes at low frequencies makes the thermal conductivity decay slower with respect to temperature than the Klemens model  $\kappa_p(T) \propto T^{-1}$  [61]. At the higher temperatures (from 300 to 600 K), the main factor increasing modal thermal conductivities, whose frequencies are lower than those of guest atoms, changes from lifetime to group velocity, as shown in Fig. 5(d). Here,  $\kappa_p^{\text{SCP}}$  at 10–20  $\text{cm}^{-1}$  increases by 44% because of the increase in group velocity, while lifetimes do not change  $\kappa_p^{\text{SCP}}$  at the same frequency range. In this temperature range, the increase in lifetimes which appear at 30–40  $\text{cm}^{-1}$ , which is located between the flat guest modes ( $\approx 20 \text{ cm}^{-1}$ ) and flat modes dominated by framework (40–50  $\text{cm}^{-1}$ ), may be more interesting. Here,  $\kappa_p^{\text{SCP}}$  at 30–40  $\text{cm}^{-1}$  increases by 2.8 times because of the increase in lifetimes. Consequently, in addition to the increase in thermal conductivity of lower-frequency phonons compared with the flat guest modes, this abnormal increase in phonon lifetimes at higher frequencies than that of the guest modes leads to the very slow decay of temperature dependence of  $\kappa(T)$ .

To gain more insights into the abnormal increase in lifetimes at high temperatures, we focused on a phonon mode at  $>30 \text{ cm}^{-1}$  whose lifetime increased the most. First, we identified that the lifetime of a phonon mode at  $\mathbf{q} = (0.00 \ 0.053, \ 0.37)$  and  $\omega = 35 \text{ cm}^{-1}$  at 300 K (see Fig. S5 in the SM [42]) increased the most from 300 to 600 K (from 1.1 to 7.1 ps). Figures 5(e) and 5(f) show, respectively, the magnitude of the three-phonon coupling matrix element, the  $|V_3|^2$  term, which is determined by eigenvectors, frequencies, and atomic masses of the scattered phonons [see Eq. (2)], and the  $|V_3|^2$  term multiplied by the SPS term at 300 and 600 K. These figures clearly show that the decrease in  $|V_3|^2$  leads to the decrease in the scattering rate and, thus, the increase in the lifetime of the target phonon mode.

#### E. Contribution of off-diagonal components

Finally, we have analyzed the contribution of coherent thermal transport. Considering this effect, we have reproduced a slower reduction of thermal conductivity of type-I BGSn above room temperature, as shown in Fig. 2. Figure 6 shows that flat bands below 60  $\text{cm}^{-1}$  mainly contribute to

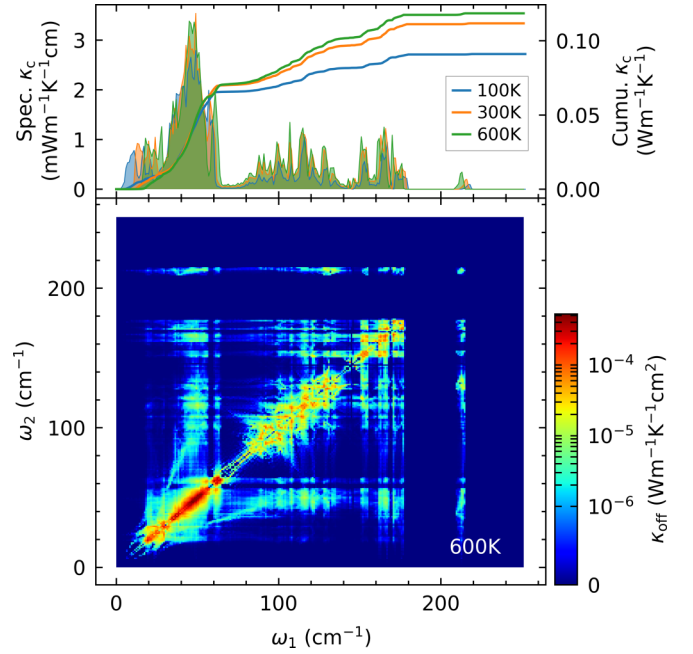


FIG. 6. Contribution of the interbranch coherent component  $\kappa_c$  of type-I BGSn. The top panel shows spectral and cumulative thermal conductivities at different temperatures, while the bottom panel shows the two-dimensional modal thermal conductivity  $\kappa_c(\omega_1, \omega_2)$  [see Eq. (3)]. To obtain the spectral and cumulative thermal conductivities (top), the contribution of mode  $q_1$  of a coupling between two modes  $q_1$  and  $q_2$  is distributed as  $c_{q_1}/(c_{q_1} + c_{q_2})$ , where  $c_q$  is the mode specific heat.

the coherent thermal transport in the overall temperature. Below 60  $\text{cm}^{-1}$ , flat modes dominated by the framework (30–60  $\text{cm}^{-1}$ ) have a larger impact on the coherent component than the flat guest modes ( $\approx 20 \text{ cm}^{-1}$ ). The figure also shows that coupling between nearly degenerate states ( $\omega_1 \simeq \omega_2$ ) has a large contribution in the low-frequency range (20–60  $\text{cm}^{-1}$ ). However, because phonons at this low-frequency range are excited at temperatures below 100 K, the contribution to  $\kappa_c(T)$  below 60  $\text{cm}^{-1}$  does not change significantly with increasing temperature when the temperature is above 100 K. Instead of the low-frequency phonons, the contribution of phonon pairs with different frequencies ( $\omega_1 \neq \omega_2$ ) at higher frequency ( $>60 \text{ cm}^{-1}$ ) increases with temperature. For example, the contribution of phonons above 60  $\text{cm}^{-1}$  increases from 31% at 100 K to 47% at 600 K. In the total lattice thermal conductivity ( $\kappa_p^{\text{SCP}} + \kappa_c$ ), the contribution of the coherent heat transport increases from 17% at 100 K to 38% at 600 K, which is not negligible.

#### IV. CONCLUSIONS

In conclusion, we have revealed the complicated effects of strong quartic anharmonicity on phonon properties of a type-I clathrate with quadruple-well potential. The whole lattice contribution, including interbranch coherent contribution, was analyzed for lattice contribution by employing first-principles anharmonic lattice dynamics combined with the SCP theory and the unified theory. The overall trend of the temperature-dependent thermal conductivity  $\kappa(T)$  has been successfully

reproduced by considering electron contribution as well as the lattice contributions. It was confirmed that the sharp increase in thermal conductivity observed in an experiment can be attributed to electron contribution and bipolar effect. It was also found that the contribution of the coherent thermal transport is distinct at high temperatures (38% at 600 K). More interestingly, we found that lattice thermal conductivity of phonons located at lower frequencies than those of flat bands of the framework ( $40\text{--}50\text{ cm}^{-1}$ ) increases with temperature, and this increase leads to the weak temperature dependence of the total lattice thermal conductivity with increasing temperature.

Detailed analysis showed that the low-frequency region ( $<40\text{ cm}^{-1}$ ) can be further divided into two regions by the flat guest modes ( $T_{2g}$  and  $E_g$  modes  $\sim 20\text{ cm}^{-1}$ ). The contribution of low-frequency phonons located below the frequency of the guest modes increases with temperature because of the increase in both of group velocities and lifetimes after the hardening of the guest modes. We found that thermal conductivities of phonons with higher frequencies than that of the guest modes start to increase above room temperature

(300 K) because of the abnormal increase in their lifetimes. This abnormal increase in the contribution of low-frequency phonons with temperature can be attributed to the decrease in the three-phonon matrix elements,  $|V_3|$  terms, with guest modes. These findings indicate that it may be possible to manipulate phonon properties by tuning phonon anharmonicity of materials by using substitutions or vacancies, which can pave a path of phonon engineering.

## ACKNOWLEDGMENTS

The numerical calculations in this paper were carried out on the facilities of the Supercomputer Center, Institute for Solid State Physics, the University of Tokyo and MASAMUNE-IMR at the Center for Computational Materials Science, Institute for Materials Research, Tohoku University (Project No. 20S0514). This paper is partially supported by Japan Society for the Promotion of Science KAKENHI Grants No. 19H00744 and No. 20K146761 and CREST Grants No. JPMJCR20Q3 and No. JPMJCR19Q3 from the Japan Science and Technology Agency.

- 
- [1] G. A. Slack, *CRC Handbook of Thermoelectrics*, edited by D. M. Rowe (CRC Press, Boca Raton, 1995), Chap. 34.
- [2] B. C. Sales, D. Mandrus, B. C. Chakoumakos, V. Keppens, and J. R. Thompson, *Phys. Rev. B* **56**, 15081 (1997).
- [3] T. Tadano and S. Tsuneyuki, *Phys. Rev. B* **92**, 054301 (2015).
- [4] M. A. Haque, S. Kee, D. R. Villalva, W.-L. Ong, and D. Baran, *Adv. Sci.* **7**, 1903389 (2020).
- [5] M. Christensen, A. B. Abrahamsen, N. B. Christensen, F. Juranyi, N. H. Andersen, K. Lefmann, J. Andreasson, C. R. H. Bahl, and B. B. Iversen, *Nat. Mater.* **7**, 811 (2008).
- [6] T. Takabatake, K. Suekuni, T. Nakayama, and E. Kaneshita, *Rev. Mod. Phys.* **86**, 669 (2014).
- [7] K. Suekuni, M. A. Avila, K. Umeo, and T. Takabatake, *Phys. Rev. B* **75**, 195210 (2007).
- [8] K. Suekuni, M. A. Avila, K. Umeo, H. Fukuoka, S. Yamanaka, T. Nakagawa, and T. Takabatake, *Phys. Rev. B* **77**, 235119 (2008).
- [9] M. Christensen, S. Johnsen, and B. B. Iversen, *Dalton Trans.* **39**, 978 (2010).
- [10] D. Weaire and R. Fhelan, *Philos. Mag. Lett.* **70**, 345 (2006).
- [11] G. S. Nolas, J. L. Cohn, G. A. Slack, and S. B. Schujman, *Appl. Phys. Lett.* **73**, 178 (1998).
- [12] J. L. Cohn, G. S. Nolas, V. Fessatidis, T. H. Metcalf, and G. A. Slack, *Phys. Rev. Lett.* **82**, 779 (1999).
- [13] B. C. Sales, B. C. Chakoumakos, R. Jin, J. R. Thompson, and D. Mandrus, *Phys. Rev. B* **63**, 245113 (2001).
- [14] Y. Takasu, T. Hasegawa, N. Ogita, M. Udagawa, M. A. Avila, K. Suekuni, I. Ishii, T. Suzuki, and T. Takabatake, *Phys. Rev. B* **74**, 174303 (2006).
- [15] K. Suekuni, Y. Takasu, T. Hasegawa, N. Ogita, M. Udagawa, M. A. Avila, and T. Takabatake, *Phys. Rev. B* **81**, 205207 (2010).
- [16] S. Christensen, M. S. Schmøkel, K. A. Borup, G. K. H. Madsen, G. J. McIntyre, S. C. Capelli, M. Christensen, and B. B. Iversen, *J. Appl. Phys.* **119**, 185102 (2016).
- [17] C. H. Lee, I. Hase, H. Sugawara, H. Yoshizawa, and H. Sato, *J. Phys. Soc. Jpn.* **75**, 123602 (2006).
- [18] W. Li and N. Mingo, *Phys. Rev. B* **89**, 184304 (2014).
- [19] T. Tadano, Y. Gohda, and S. Tsuneyuki, *Phys. Rev. Lett.* **114**, 095501 (2015).
- [20] T. Tadano and S. Tsuneyuki, *Phys. Rev. Lett.* **120**, 105901 (2018).
- [21] X. Zheng, S. Y. Rodriguez, and J. H. Ross, *Phys. Rev. B* **84**, 024303 (2011).
- [22] I. Zerec, V. Keppens, M. A. McGuire, D. Mandrus, B. C. Sales, and P. Thalmeier, *Phys. Rev. Lett.* **92**, 185502 (2004).
- [23] D. J. Hooton, *Philos. Mag.* **3**, 49 (1958).
- [24] T. Tadano and S. Tsuneyuki, *J. Phys. Soc. Jpn.* **87**, 041015 (2018).
- [25] M. Simoncelli, N. Marzari, and F. Mauri, *Nat. Phys.* **15**, 809 (2019).
- [26] G. Kresse and J. Furthmüller, *Phys. Rev. B* **54**, 11169 (1996).
- [27] J. P. Perdew, K. Burke, and M. Ernzerhof, *Phys. Rev. Lett.* **77**, 3865 (1996).
- [28] P. E. Blöchl, *Phys. Rev. B* **50**, 17953 (1994).
- [29] G. Kresse and D. Joubert, *Phys. Rev. B* **59**, 1758 (1999).
- [30] H. Anno, H. Yamada, T. Nakabayashi, M. Hokazono, and R. Shirataki, *J. Phys.: Conf. Ser.* **379**, 012007 (2012).
- [31] M. A. Avila, K. Suekuni, K. Umeo, H. Fukuoka, S. Yamanaka, and T. Takabatake, *Appl. Phys. Lett.* **92**, 041901 (2008).
- [32] K. Parlinski, Z. Q. Li, and Y. Kawazoe, *Phys. Rev. Lett.* **78**, 4063 (1997).
- [33] W. G. Hoover, *Phys. Rev. A* **31**, 1695 (1985).
- [34] T. Hastie, R. Tibshirani, and M. Wainwright, *Statistical Learning with Sparsity: The Lasso and Generalizations* (CRC Press, Boca Raton, 2015).
- [35] I. Errea, M. Calandra, and F. Mauri, *Phys. Rev. B* **89**, 064302 (2014).



- [36] R. J. Hardy, *Phys. Rev.* **132**, 168 (1963).
- [37] S. Tamura, *Phys. Rev. B* **27**, 858 (1983).
- [38] P. E. Blöchl, O. Jepsen, and O. K. Andersen, *Phys. Rev. B* **49**, 16223 (1994).
- [39] T. Tadano, Y. Gohda, and S. Tsuneyuki, *J. Phys.: Condens. Matter* **26**, 225402 (2014).
- [40] Y. Saiga, K. Suekuni, B. Du, and T. Takabatake, *Solid State Commun.* **152**, 1902 (2012).
- [41] G. K. H. Madsen, J. Carrete, and M. J. Verstraete, *Comput. Phys. Commun.* **231**, 140 (2018).
- [42] See Supplemental Material at <http://link.aps.org/supplemental/10.1103/PhysRevB.106.024303> for detailed descriptions.
- [43] F. Oba and Y. Kumagai, *Appl. Phys. Express* **11**, 060101 (2018).
- [44] N. P. Blake, D. Bryan, S. Lattner, L. Møllnitz, G. D. Stucky, and H. Metiu, *J. Chem. Phys.* **114**, 10063 (2001).
- [45] E. N. Nenghabi and C. W. Myles, *Phys. Rev. B* **77**, 205203 (2008).
- [46] M. Ångqvist, D. O. Lindroth, and P. Erhart, *Chem. Mater.* **28**, 6877 (2016).
- [47] M. Ångqvist and P. Erhart, *Chem. Mater.* **29**, 7554 (2017).
- [48] D. O. Lindroth, J. Brorsson, E. Fransson, F. Eriksson, A. Palmqvist, and P. Erhart, *Phys. Rev. B* **100**, 045206 (2019).
- [49] T. Mori, K. Iwamoto, S. Kushibiki, H. Honda, H. Matsumoto, N. Toyota, M. A. Avila, K. Suekuni, and T. Takabatake, *Phys. Rev. Lett.* **106**, 015501 (2011).
- [50] J. Shiomi, K. Esfarjani, and G. Chen, *Phys. Rev. B* **84**, 104302 (2011).
- [51] F. Bridges and L. Downward, *Phys. Rev. B* **70**, 140201 (2004).
- [52] L. Xie, J. H. Feng, R. Li, and J. Q. He, *Phys. Rev. Lett.* **125**, 245901 (2020).
- [53] Y. Xia, V. I. Hegde, K. Pal, X. Hua, D. Gaines, S. Patel, J. He, M. Aykol, and C. Wolverton, *Phys. Rev. X* **10**, 041029 (2020).
- [54] M. A. Avila, K. Suekuni, K. Umeo, H. Fukuoka, S. Yamanaka, and T. Takabatake, *Phys. Rev. B* **74**, 125109 (2006).
- [55] T. Nakayama and E. Kanashita, *EPL* **84**, 66001 (2008).
- [56] D. G. Cahill, S. K. Watson, and R. O. Pohl, *Phys. Rev. B* **46**, 6131 (1992).
- [57] S. Paschen, W. Carrillo-Cabrera, A. Bienten, V. H. Tran, M. Baenitz, Y. Grin, and F. Steglich, *Phys. Rev. B* **64**, 214404 (2001).
- [58] B. Poudel, Q. Hao, Y. Ma, Y. Lan, A. Minnich, B. Yu, X. Yan, D. Wang, A. Muto, D. Vashaee, X. Chen, J. Liu, M. S. Dresselhaus, G. Chen, and Z. Ren, *Science* **320**, 634 (2008).
- [59] M. Kashiwagi, Y. Liao, S. Ju, A. Miura, S. Konishi, T. Shiga, T. Kodama, and J. Shiomi, *ACS Appl. Energy Mater.* **2**, 7083 (2019).
- [60] M. Ohnishi and J. Shiomi, *APL Mater.* **7**, 013102 (2019).
- [61] P. G. Klemens, *Proc. Phys. Soc. A* **68**, 1113 (1955).